Preparation of porous ZrO_2/Al_2O_3 macrobeads from ion-exchange resin templates

M.-L. Wang · C.-H. Wang · W. Wang

Abstract In this work, we will report a method to prepare porous ZrO_2 and ZrO_2/Al_2O_3 macrobeads using cation-exchange resins with sulfonate groups as templates. The preparation process involves metal ion-loading, ammonia-precipitation, and calcination at an appropriate temperature. Several characterization methods, such as TGA, XRD, SEM with EDX, TEM and N_2 adsorption and desorption, were used to characterize the ZrO_2 and ZrO_2/Al_2O_3 macrobeads. The results showed that the porous structures of the resin templates were negatively duplicated in the two kinds of macrobeads. We found the following interesting results: (1) The ZrO_2/Al_2O_3 macrobeads are composed of tetragonal zirconia nanocrystals that are more technologically important, while the pure ZrO_2 macrobeads consist of a mixture of tetragonal and monoclinic zirconia. (2) In the ZrO_2/Al_2O_3 macrobeads, the size of ZrO_2 nanocrystals is about 5 nm smaller than that (about 19 nm) found in the pure ZrO_2 macrobeads. (3) The ZrO_2/Al_2O_3 macrobeads have more mesopores and, therefore, have a larger surface area than the pure ZrO_2 macrobeads. These oxide macrobeads will have potential applications in catalysis by taking advantage of their macrobeads shape and pores structure.

Introduction

Materials based on zirconium dioxide (ZrO_2) are very important because of their wide applications in ceramics, oxygen sensors, catalysts, and catalyst supports [1–4].

M.-L. Wang · C.-H. Wang · W. Wang (✉)
The Key Laboratory of Functional Polymer Materials of Ministry of Education and Institute of Polymer Chemistry, College of Chemistry, Nankai University, Tianjin 300071, China
e-mail: weiwang@nankai.edu.cn

Since ZrO_2 has both acid and base active centers on its surface [5], it has been used as a key active component of some catalysts for various processes such as dehydration, isomerization, alkylation, and selective and full oxidation of hydrocarbons [6–8]. Conventionally, ZrO_2 used in catalysis process is often in the form of powders [1–8]. However, it is trivial to completely remove catalyst powders from the products after the reaction and the performance of products could be strongly affected by residual catalysts. Therefore, ZrO_2 porous macrobeads with sizes over a couple of hundred micrometers will be a good candidate. This is because porous macrobeads can not only provide a high surface area with more ZrO_2 active centers on the pore surface, but also be easily removed from product solution by a simple filtration process. Although several efforts have been reported to prepare porous metal oxide macrobeads using the corresponding alkoxides as precursors [9–19], the study on ZrO_2 is still limited [20]. One of the reasons for the failure in preparation ZrO_2 porous macrobeads is that zirconium alkoxide is too reactive to be handled. Recently, Konishi et al. [21] successfully prepared porous ZrO_2 monoliths through a relatively complicated method, which involves alkoxy-derived sol–gel process, phase separation and solvothermal process. The precursor they used is zirconium propoxide. During preparation, *N*-methylformamide should be added to the reaction system to slow down the gelation of ZrO_2, so the reaction conditions had to be carefully controlled. The prepared ZrO_2 products are cylindrical monoliths. Therefore, it is still a challenge to prepare porous ZrO_2 macrobeads by means of a relatively simple method using other zirconium compounds as precursors, which can be easily handled, like $ZrOCl_2$.

Nowadays, it is well-known that ZrO_2 can possess three crystalline phases, i.e., cubic, tetragonal and monoclinic

polymorphs [22]. The monoclinic phase, which is stable at room temperature, is transformed to tetragonal at 1170 °C, and then to cubic at 2370 °C. But the technologically more important cubic and/or tetragonal zirconias are not stable in bulk forms at ambient conditions. To obtain cubic or tetragonal zirconia that is stable at room temperature, two methods have been explored. One is to incorporate Mg^{2+}, Ca^{2+}, and Y^{3+}, which are compatible with ZrO_2, into zirconia crystal lattice to minimize the free energy of cubic and tetragonal phases [23, 24]. Another method is to decrease the particle size of ZrO_2 crystals to the 30 nm range [25]. It is found that adding even small amounts of Al_2O_3, which are not compatible with ZrO_2 below 1400 °C, can limit the size of ZrO_2 crystals [23]. Therefore, ZrO_2 nanocrystals in some mixtures of ZrO_2/Al_2O_3 have been prepared in the form of pure tetragonal phase.

We have previously demonstrated a simple route to prepare hierarchically porous Fe_2O_3, Al_2O_3, and TiO_2 macrobeads, using macroporous cation-exchange resins with sulfonic acid groups as templates and the corresponding metal salts of inorganic acids as precursors [26]. This method has at least three advantages: (1) The templates and precursors, are all commercially available and cheap in price. (2) The metal ions are fixed into the pore surface of the resins via counterion interaction that is strong enough to endure water washing, therefore the excess metal ions in the inner part and at outer surface of resin can be removed by washing. As a result, the obtained metal oxide macrobeads are free of a dense cover at the macrobead surface. (3) The crystalline framework in the obtained macrobeads will have high structural stability at higher temperature and/or other rigorous conditions. Herein, we extend this method to the preparation of ZrO_2 porous macrobeads. The as-prepared macrobeads are composed of ZrO_2 with two crystalline phases, monoclinic and tetragonal, and the surface area of the porous macrobeads is about 40 m^2/g, which is not as high as those reported in the Ref. [27]. The new challenge is to prepare ZrO_2 porous macrobeads with a pure tetragonal crystalline phase and higher surface area. In our work we easily achieve this goal by mixing Al_2O_3 with ZrO_2. In order to prepare the ZrO_2/Al_2O_3 macrobeads, the $Al(H_2O)_6^{3+}$ ions will be firstly introduced into the resin via an ion-exchange process. After an ammonia treatment the Al^{3+} ions in the resin will be transformed into an oligomeric $Al(OH)_3$ precipitate and then $(ZrO)^{2+}$ ions are reloaded into the resin pores. After another ammonia treatment, we can obtain $(Zr(OH)_4)/Al(OH)_3/resin$ composite beads. Finally, we prepare the targeted ZrO_2/Al_2O_3 porous macrobeads by calcination at high temperature. Our findings show that the crystalline structure, pore structure, and surface area of the ZrO_2 macrobeads will be improved after mixed with Al_2O_3.

Experimental

Materials

A strongly acidic cation-exchange resin with sodium sulfonate group and spherical morphology (D72, 30–50 mesh) was used in this work. It was purchased from the Chemistry Plant of Nankai University. The charged form of the resin was reversed from Na^+ to H^+ by a treatment with 10 wt% HCl solution. Typically, D72 was made by sulfonation of porous polymer beads which are composed of poly (styrene-co-divinylbezene). The divinylbenzene was used as cross-linking agent and the degree of cross-linking is about 8%. Ion-exchange capacity of D72 is 4.4 mmol/g or 1.4 mmol/mL. The inner structure of D72 was shown in our previous work [26]. Typically, D72 beads have amorphous walls and pores with size distribution of 10–600 nm. The precursor solutions used for the preparation of the oxide macrobeads were $ZrOCl_2$ and $Al(NO_3)_3$ aqueous solutions.

Preparation of macrobeads

The pure ZrO_2 macrobeads were prepared via the following steps: $(ZrO)^{2+}$ ion-loading, ammonia-precipitation and calcination. Typically, 10 g of the H^+-type ion-exchange resins, D72, were treated with 300 mL of an aqueous solution of $ZrOCl_2$ (0.1 M) to replace H^+ with $(ZrO)^{2+}$ to form a $(ZrO)^{2+}$–D72 complex. The composite resins were washed well with deionized water and then treated with 30 mL of an ammonia solution (1.0 M) to precipitate $(ZrO)^{2+}$ as oligomeric $Zr(OH)_4$ in the pores of the D72 resins. Then the obtained $Zr(OH)_4$–D72 composite resins were dried in air at 120 °C for 2 h and finally calcined at 600 °C for 8 h.

The preparation of the mixed ZrO_2/Al_2O_3 macrobeads involved Al^{3+} ion-loading, ammonia-precipitation, and the $(ZrO)^{2+}$ ion-reloading, ammonia-precipitation and final calcination steps. Generally, 10 g of D72 resins were treated with 300 mL of an aqueous solution of $Al(NO_3)_3$ followed by thorough water washing. Then 30 mL of the ammonia solution (1.0 M) was added to the Al^{3+}–D72 resins to bring about the $Al(OH)_3$ precipitation in the pores of the D72 resins. The $Al(OH)_3$–D72 composite resins were washed well using a large amount of deionized water. Then 300 mL $ZrOCl_2$ (0.1 M) were added into the composite resins so the $(ZrO)^{2+}$ ions were reloaded. These $(ZrO)^{2+}$–$Al(OH)_3$–D72 resins were again washed with deionized water and then treated again with 30 mL of the ammonia solution (1.0 M). The obtained $Zr(OH)_4/Al(OH)_3$–D72 composite resins were dried in air at 120 °C for 2 h and finally calcined at 600 °C for 8 h.

Measurements

Thermogravimetric analysis (TGA) was conducted using a NETZSCH TG209 thermoanalyzer in a 10 mL/min nitrogen flow rate and a heating rate of 10 °C/min. The weight contents of Zr and Al in ZrO_2/Al_2O_3 beads were determined by Inductive Coupled Plasma Mass Spectrometry (ICP-MS). The ZrO_2/Al_2O_3 beads were milled and then digested using 1:1 mixture of Nitric acid and Hydrofluoric acid. The Zr and Al contents in the digested sample can be measured by ICP-MS using corresponding inner standard. X-ray diffraction (XRD) experiments were carried out using a Rigaku D/Max-2500 X-ray diffractometer using Cu Kα radiation. The average crystal size of the sample was estimated by the Scherrer's formula [28], which is a technique based on measuring the full width of X-ray diffraction peaks at the half maximum height of the peak (FWHM). The Scherrer's formula is $t = 0.94 \times \lambda/B \times \cos\theta$ where t is the average crystal size, λ is the wavelength of Cu Kα radiation, B is the FWHM, and θ is the half of the diffraction angle, 2θ. The contribution to the peak broadening from the instrumental broadening was subtracted by the help of a standard silicon sample, using the formula $B^2 = B_1^2 - B_2^2$, where B_1 is measured peak and B_2 is instrumental broadening contribution. The optical microscopy images were obtained under reflected light mode using an Olympus optical microscope equipped with a digital camera. Scanning electron microscopy (SEM) experiments were conducted on a JEOL JSM-6700F field emission SEM equipped with an energy dispersive X-ray (EDX) spectroscopy analyzer. The samples were coated with gold prior to analysis. Transmission electron microscopy (TEM) and high-resolution transmission electron microscopy (HRTEM) images were recorded using a Tecnai-$G^2$20 transmission electron microscope operated at an accelerating voltage of 200 kV. The ultrasonic technique was used to well disperse the milled oxide beads in water/ethanol solution. Several drops of dispersion were deposited on a carbon coated copper grid for TEM measurement. N_2 adsorption and desorption measurements were performed at 77 K using a Micromeritics TriStar 3000 analyzer. The specific surface area was calculated using the Brunauer–Emmett–Teller (BET) method using a linear plot over the range $P/P_0 = 0.06-0.20$. Mesopore volumes were determined from the amount of N_2 adsorbed at $P/P_0 = 0.99$.

Results and discussion

After metal ion-exchange and ammonia-precipitation process, the $Zr(OH)_4$–D72 and $Zr(OH)_4/Al(OH)_3$–D72 composite resins were obtained. We firstly determined the calcination temperature of each composite via TGA

characterization. Figure 1 presents the TGA curves of the two composites. They show a complete loss of water and polymer matrix at a temperature of about 600 °C. Their residual weights are about 38% for $Zr(OH)_4/Al(OH)_3$–D72, and about 19% for $Zr(OH)_4$–D72. This difference confirms the loading of two metal ions in the former composite. The TGA characterization helps us set the lowest calcination temperature of the two composites at 600 °C to dehydrate the metal hydroxide species as well as to completely remove the polymer template.

To determine the composition of ZrO_2/Al_2O_3 in the macrobeads, we carried out EDX measurement, as shown in Fig. 2. The three peaks in the EDX spectrum correspond to the O, Al, and Zr elements, respectively. No other elements were found. This indicates that the S, C, and N elements in the composite resins were completely eliminated during the calcination. Based on the phase diagram of the alumina–zirconia binary system, alumina and zirconia are immiscible and they do not react below 1400 °C [29, 30]. Therefore, we believe that the macrobeads are composed of a simple
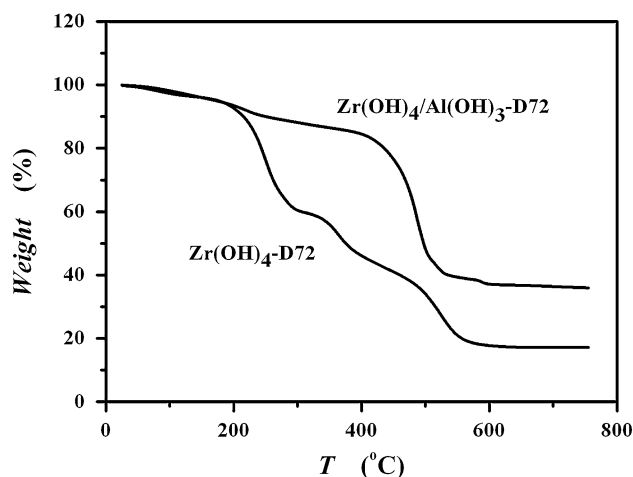
Fig. 1 TGA curves of the $Zr(OH)_4$–D72 and $Zr(OH)_4/Al(OH)_3$–D72 composite resins

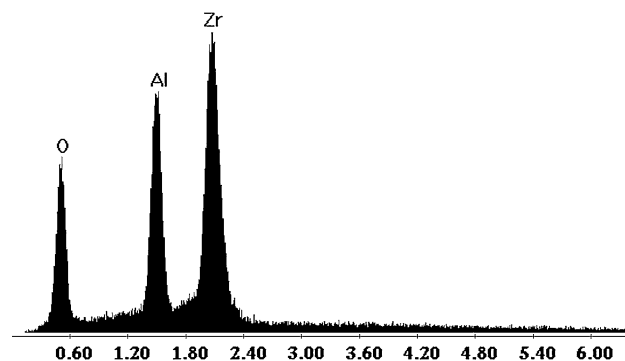**Fig. 2** EDX spectrum of the ZrO_2/Al_2O_3 macrobeads

mixture of zirconia and alumina that will be further proved in the following XRD characterization.

During preparation of the ZrO_2/Al_2O_3 macrobeads, we used ammonia as the weak base to transform Al^{3+} ions fixed in the pore surface of the resin into $Al(OH)_3$ precipitate and to simultaneously free the sulfonate group that could further complex with $(ZrO)^{2+}$ ions. Theoretically, 1 mol of $R–SO_3^-$ can exchange with 0.33 mol of Al^{3+} and 0.5 mol of $(ZrO)^{2+}$. So the mole ratio of Zr to Al in the final ZrO_2/Al_2O_3 macrobeads should be $0.5/0.33 = 1.5$ if all the $R–SO_3^-$ could be free and further complex with $(ZrO)^{2+}$ after the first ammonia-precipitation process. The result of ICP measurement reveals that the weight contents of ZrO_2 and Al_2O_3 in the final ZrO_2/Al_2O_3 macrobeads are 52 and 47%, respectively. Corresponding mole ratio of Zr to Al is 0.92. The possible reason for less Zr content than theoretical value may be that some of the $R–SO_3^-$ could be wrapped by the $Al(OH)_3$ precipitate after addition of ammonia into the Al^{3+} loaded resin. Clearly, those wrapped sulfonate group can not be complexed further with any $(ZrO)^{2+}$.

Figure 3 shows powder XRD patterns of the as-synthesized metal oxide products. For the ZrO_2/Al_2O_3 macrobead, there are four broadened peaks centered at about $2\theta = 30.1°, 34.9°, 50.2°,$ and $59.6°$, respectively, and they correspond to (111), (200), (220), and (311) lattice planes of tetragonal zirconia. The appearance of these peaks indicates that the macrobead is composed of almost pure tetragonal phase of crystalline zirconia. However, no peaks can be assigned to Al_2O_3 crystals, implying an amorphous or poorly crystalline structure formed. The amorphous alumina phase is also reported in the powdered mixtures of ZrO_2 and Al_2O_3 [31]. The average size of the zirconia

Fig. 3 XRD patterns of the ZrO_2 and ZrO_2/Al_2O_3 macrobeads, with the Miller index of tetragonal zirconia indicated by *number* and diffraction peaks of monoclinic zirconia indicated by *asterisk*

crystals, estimated according to the Scherrer's formula [28], was 4.9 nm. On the other hand, the XRD pattern of the ZrO_2 macrobeads exhibits three strong peaks together with several relatively weak peaks. According to JCPDS cards (No. 17-0923 and 37-1484), the strong peaks can be attributed to the diffractions of the (111), (220), and (311) planes of tetragonal zirconia crystals, respectively, and the other weak peaks can be assigned as diffraction peaks of monoclinic zirconia. The results show that the ZrO_2 macrobeads are composed of a mixture of two different crystalline phases, namely tetragonal and monoclinic zirconia. Based on the Scherrer formula and the diffraction peaks of (111) crystal plane, we estimate the size of the ZrO_2 crystals to be 15 nm, which is larger than that found in ZrO_2/Al_2O_3 macrobeads. Garvie and Gross [25] have reported that ZrO_2 can be stabilized in the tetragonal crystal structure at room temperature when its size decreased below a critical size of 30 nm, due to the lower surface energy of tetragonal structure compared to the monoclinic structure. The ZrO_2 macrobeads, with their average nanocrystals size of 15 nm, still contain some monoclinic crystals. This may be explained by the fact that there are some crystals with sizes over 15 nm, even 30 nm, in the ZrO_2 macrobeads. When the size of zirconia crystals decreases to 5 nm in the ZrO_2/Al_2O_3 macrobeads, however, all the zirconia crystals are stabilized in the tetragonal form.

After calcination of the corresponding metal hydroxide-resin composite macrobeads, $Zr(OH)_4$–D72 and $Zr(OH)_4/Al(OH)_3$–D72, the as-synthesized metal oxides well maintained the bead shape of the parent resin, which was evidenced by optical microscopy observations. Figure 4a and b exhibits typical images of the metal oxide macrobeads, from which we can see that they both have good bead morphology with few cracks. The corresponding size distributions of the macrobeads and the parent resin, D72, are shown in Fig. 4c. They all have similar distributions implying a conformable change from composite beads to oxide ones. The average size of the ZrO_2/Al_2O_3 beads ($\sim450\ \mu m$) is the same as that of D72 ($\sim450\ \mu m$), while the average size of the ZrO_2 macrobeads decreased to $\sim330\ \mu m$. The results show that shrinkage occurred in the preparation of the lower loaded ZrO_2 macrobeads, but not in the preparation of the ZrO_2/Al_2O_3 macrobeads. The reason for the shrinkage may be the crystallization and Oswald ripening of ZrO_2 particles during calcination. For the preparation of the ZrO_2/Al_2O_3 macrobeads, however, the amorphous Al_2O_3 phase hindered the Oswald ripening of ZrO_2 nanocrystals, thus the size and packing of the nanocrystals kept almost unchanged even at high calcination temperature.

SEM images in Fig. 5 show the pore structure of the two macrobeads. Both macrobeads have relatively thick and
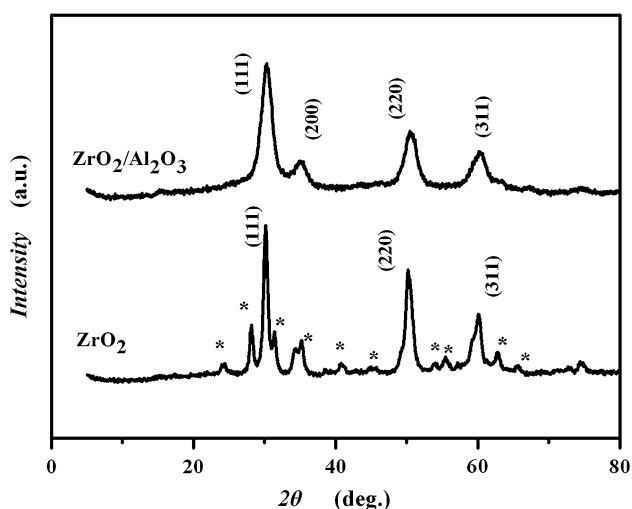
rough frameworks as well as a large amount of voids between and within these frameworks. The pore size between frameworks is in the range of 5–50 nm. Our SEM
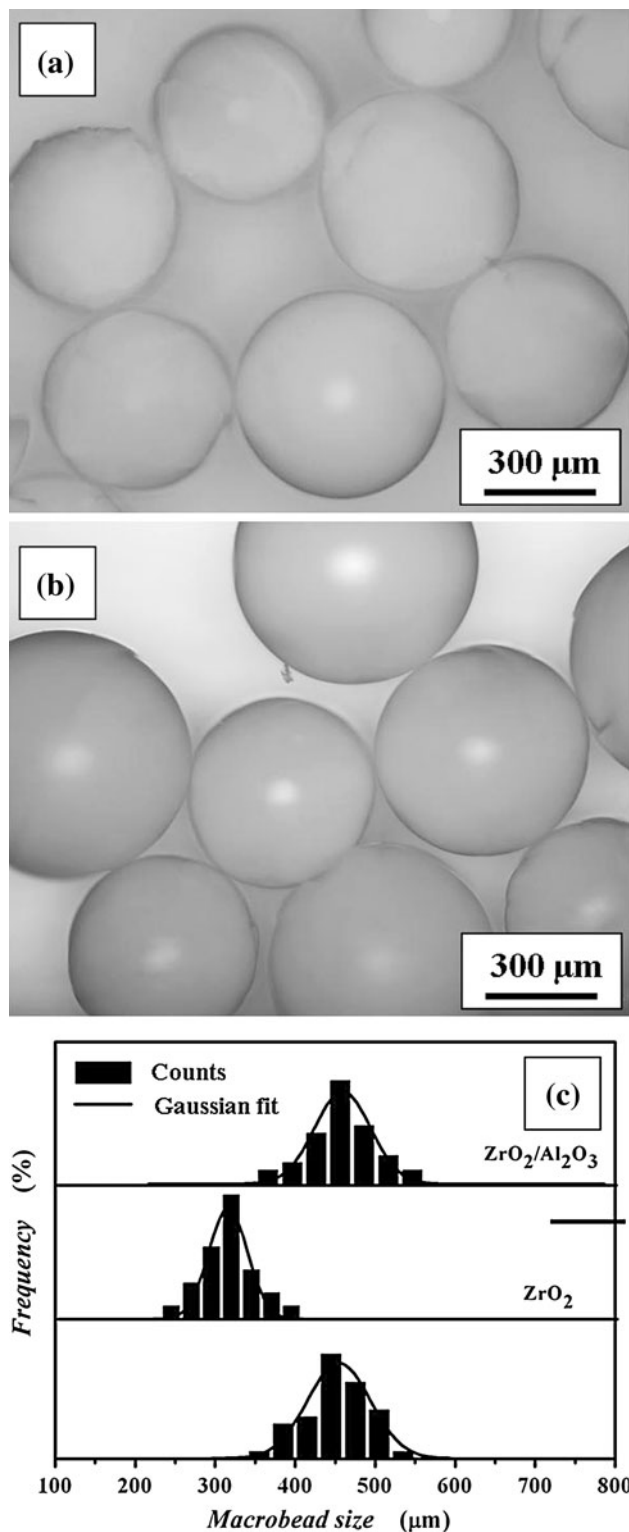

Fig. 4 Optical images of the ZrO$_2$ macrobeads (a) and the ZrO$_2$/Al$_2$O$_3$ macrobeads (b). c The size distributions of the two macrobeads together with that of the parent resin templates, D72

characterization shows that the pore size in the parent D72 resin distributes in the range of 10–600 nm (images not shown) [26]. The porous characteristic of the metal oxide beads is similar to the D72 resin, indicating that the main porous feature in the metal oxide beads is negatively duplicated from that of the D72 template. However, the pore size might be altered during the calcination process because of the chemical and physical changes from metal hydroxide/resin composites into metal oxides. In addition, the pores within the frameworks are much smaller in size than those between the frameworks, therefore, it is hard to clearly identify those pores by SEM due to the resolution limitation.

Figure 6 exhibits the typical TEM and HRTEM images of the two oxide macrobeads. In the ZrO$_2$ macrobeads, the ZrO$_2$ nanocrystals have a size in the range of 10–30 nm (Fig. 6a, b). Loose packing of these nanocrystals creates voids; however, these voids are relatively irregular in shape as the crystals pack irregularly. On the other hand, the ZrO$_2$ nanocrystals in the ZrO$_2$/Al$_2$O$_3$ macrobeads have a size of about 5 nm and they are packed in relatively ordered manner (Fig. 6c), so the voids between these crystals look
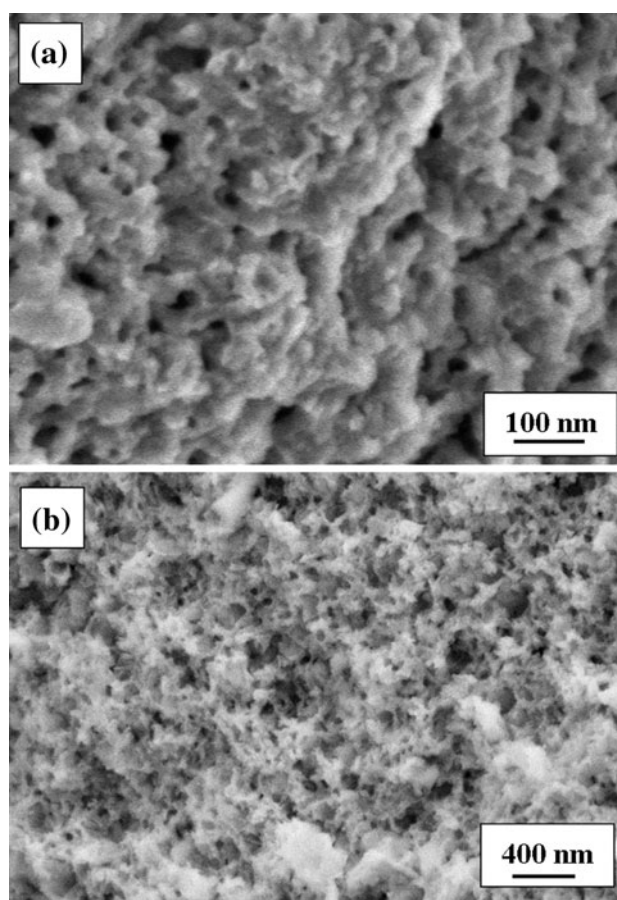

Fig. 5 SEM images of inner pore structure of the ZrO$_2$ macrobeads (a) and the ZrO$_2$/Al$_2$O$_3$ macrobeads (b)

more ordered. The size of those voids is approximately 3–7 nm. The fine crystal structure of the ZrO_2 nanocrystals in the ZrO_2/Al_2O_3 mixture is disclosed by the HRTEM image in Fig. 6d showing regular projection lines of the (111) lattice plane of tetragonal zirconia. The average distance between each line is 0.296 nm, consistent with the result of the XRD characterization.

We carefully measured ZrO_2 particles size from over 20 TEM images and obtained size distributions of the ZrO_2. The results are presented in Fig. 7. The average sizes of the ZrO_2 particles are approximately 19 and 5 nm in the ZrO_2 and ZrO_2/Al_2O_3 macrobeads, respectively. They are very close to the size obtained by the XRD characterization. It is important to note again that after mixed with Al_2O_3, the size of the ZrO_2 nanocrystals decreased from 19 to 5 nm. The existence of Al_2O_3 is generally thought to be an important factor that hinders the crystal growth of ZrO_2 during the calcination process [25, 32]. The smaller size of the ZrO_2 nanocrystals further makes the tetragonal zirconia phase stable at room temperature in our study.

To determine the surface area and pore structure of the two macrobeads, we carried out N_2-sorption measurements. Figure 8 shows the adsorption and desorption isotherms of the ZrO_2 and ZrO_2/Al_2O_3 macrobeads, together with the corresponding pore-size distributions (PSDs). Both isotherms exhibit type III characteristics with a type H3 loop, which is usually indicative of broad size distributions and large mesopores. The existence of large mesopores has been confirmed by our SEM characterization. The PSDs from the adsorption branch of the isotherms using the Barrett–Joyner–Halenda (BJH) method reveal that the mesopore sizes of ZrO_2 and ZrO_2/Al_2O_3 are both in the range of 2–40 nm and pores larger than 40 nm are also observed with small contribution. However, the mesopore volume (V_{meso}) and the specific surface area (S_{BET}) determined from the isotherms differ greatly from each other. S_{BET} is 40.4 m^2/g for the ZrO_2 macrobeads and 131.3 m^2/g for the ZrO_2/Al_2O_3 macrobeads, while V_{meso} is 0.09 cm^3/g and 0.20 cm^3/g for the ZrO_2 and ZrO_2/Al_2O_3 macrobeads, respectively. The increases of the S_{BET} and V_{meso} values in
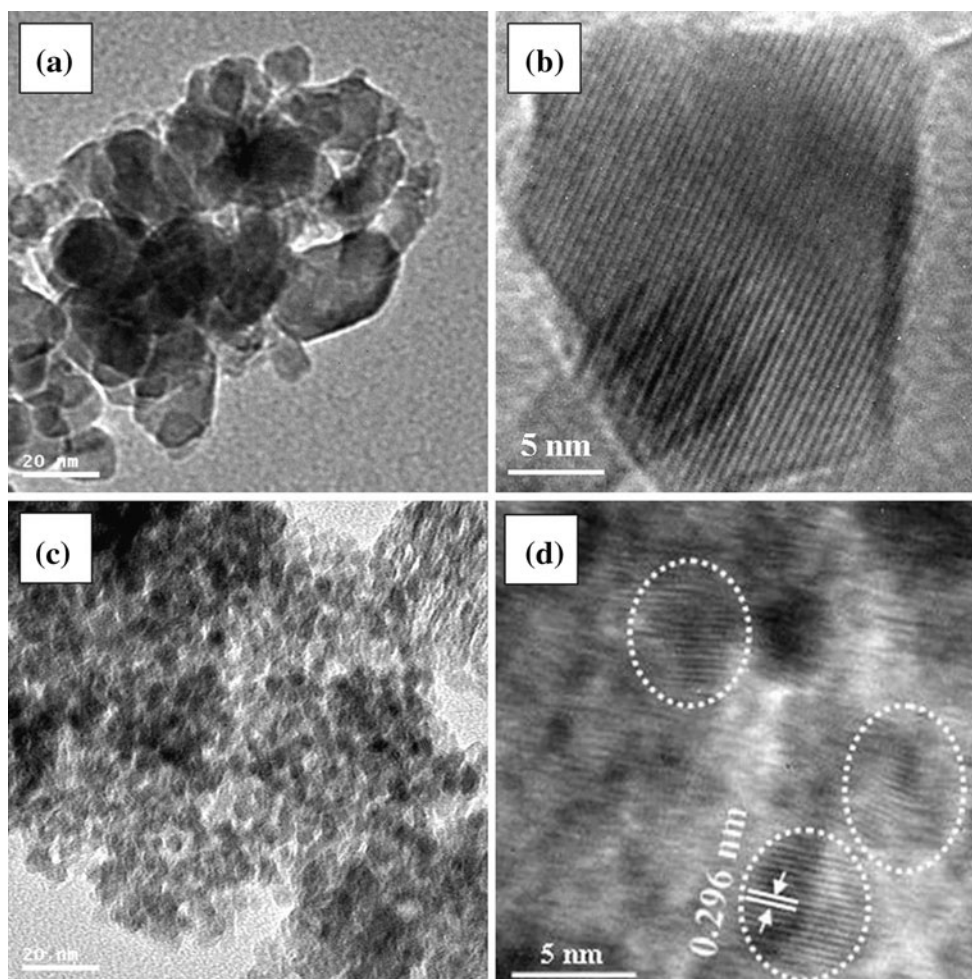

Fig. 6 TEM (**a**) and HRTEM (**b**) images of nanocrystals in the ZrO_2 macrobeads. TEM (**c**) and HRTEM (**d**) images of ZrO_2 nanocrystals in the ZrO_2/Al_2O_3 macrobeads
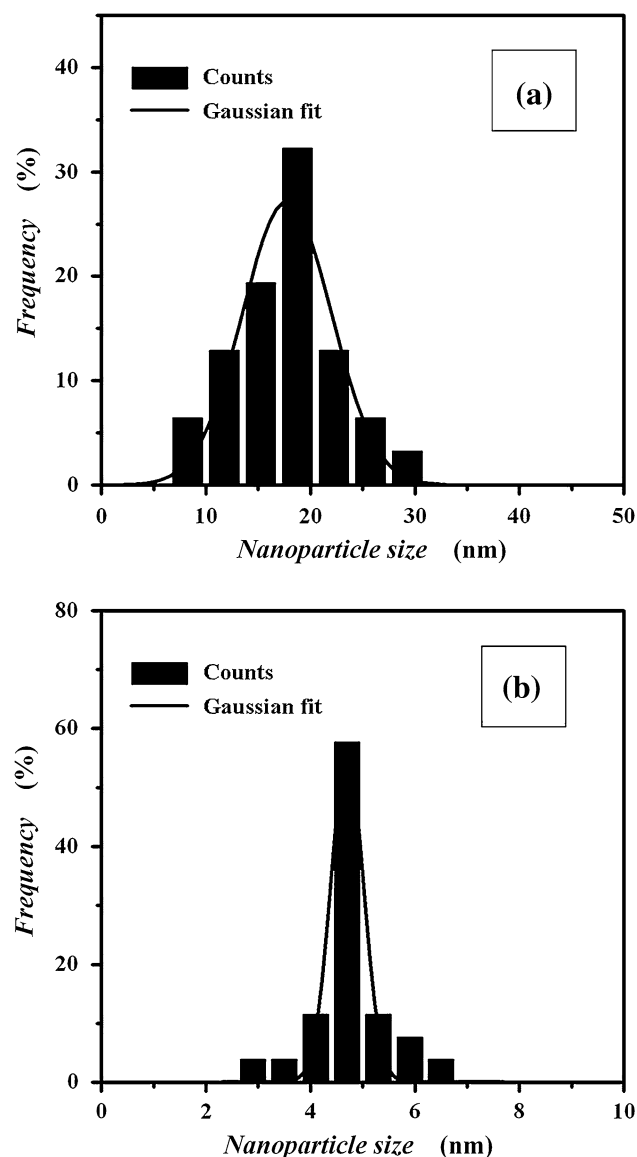
Fig. 7 Nanocrystal size distribution of the ZrO_2 (**a**) and ZrO_2/Al_2O_3 (**b**) macrobeads

Fig. 8 a N_2 adsorption–desorption isotherms and b BJH pore-size distributions of the ZrO_2 and ZrO_2/Al_2O macrobeads

the ZrO_2/Al_2O_3 macrobeads indicate the formation of fine and more voids. In the mixture of Al_2O_3 with ZrO_2, the Al_2O_3 amorphous phase hindered the Oswald ripening of the ZrO_2 nanocrystals during calcination, so those nanocrystals can keep their smaller size and relatively ordered packing and the fine voids between nanocrystals are much more numerous than those in the ZrO_2 macrobeads. This accounts for the higher S_{BET} and V_{meso} in the ZrO_2/Al_2O_3 macrobeads.

Conclusion

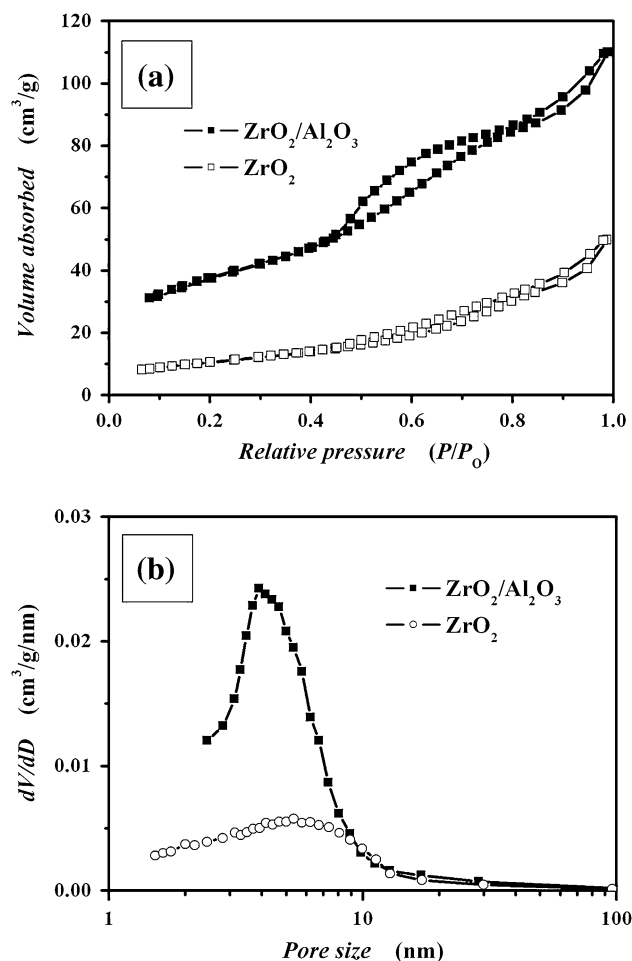In conclusion, we have prepared the two porous ZrO_2 and ZrO_2/Al_2O_3 macrobeads using ion-exchange resins as hard templates. After metal ion-loading, ammonia-precipitation, and calcination, we obtained the targeted metal oxides that keep the bead shape and pore structure of the resin template. For the ZrO_2/Al_2O_3 beads, there are many improvements in properties compared with those of the pure ZrO_2 beads: (1) In the ZrO_2/Al_2O_3 macrobeads tetragonal zirconia nanocrystals, which are more technologically important, are formed, while in the ZrO_2 macrobeads a mixture of tetragonal and monoclinic zirconia is formed. (2) The size of the ZrO_2 nanocrystals decreases from 19 to 5 nm upon mixing with Al_2O_3. (3) The ZrO_2/Al_2O_3 macrobeads have more mesopores with fine structure and, therefore, have a larger surface area than the ZrO_2 macrobeads. The two oxide macrobeads have potential applications in catalysis by taking advantage of their macrobeads shape and pores characteristics.

References

1. Garvie RC, Hannink RH, Pascoe RT (1975) Nature 258:703
2. León C, Lucía ML, Santamaria J (1997) Phys Rev B 55:882
3. Haw JF, Zhang J, Shimizu K, Venkatraman TN, Luigi DP, Song W, Barich DH, Nicholas JB (2000) J Am Chem Soc 122:12561
4. Jung KT, Bell AT (2002) Catal Lett 80:63
5. Jung KT, Bell AT (2000) J Mol Catal A: Chem 163:27
6. Ivanova AS (2001) Kinet Katal 42:354
7. Wang XH, Lu GZ, Guo Y, Jiang LZ, Guo YH, Li CZ (2009) J Mater Sci 44:1294. doi:10.1007/s10853-009-3275-4
8. Reddy BM, Reddy GK, Ganesh I, Ferreira JMF (2009) J Mater Sci 44:2743. doi:10.1007/s10853-009-3358-2
9. Meyer U, Larsson A, Hentze HP, Caruso RA (2002) Adv Mater 14:1768
10. Shchukin DG, Caruso RA (2004) Chem Mater 16:2287
11. Deshpande AS, Shchukin DG, Ustinovich E, Antonetti M, Caruso RA (2005) Adv Funct Mater 15:239
12. Zhang H, Hardy GC, Khimyak YZ, Rosseinsky MJ, Cooper AI (2004) Chem Mater 16:4245
13. Zhang H, Cooper AI (2005) Ind Eng Chem Res 44:8707
14. Tosheva L, Valtchev V, Sterte J (2000) Microporous Mesoporous Mater 35–36:621
15. Tosheva L, Valtchev V, Sterte J (2000) J Mater Chem 10:2330
16. Tosheva L, Parmentier J, Saadallah S, Vix-Guterl C, Valtchev V, Patarin J (2004) J Am Chem Soc 126:13624
17. Tiemann M (2008) Chem Mater 20:961
18. Wang YJ, Price AD, Caruso F (2009) J Mater Chem 19:6451
19. Pan JH, Dou H, Xiong Z, Xu C, Ma J, Zhao XS (2010) J Mater Chem 20:4512
20. Sizgek GD, Griffith CS, Sizgek E, Luca V (2009) Langmuir 25:11874
21. Konishi J, Fujita K, Oiwa S, Nakanishi K, Hirao K (2008) Chem Mater 20:2165
22. Joo J, Taekyung Y, Kim YW, Park HM, Wu F, Zhang JZ, Hyeon T (2003) J Am Chem Soc 125:6553
23. Garvie RC (1978) J Phys Chem 82:218
24. Hu LF, Wang CA, Huang Y (2010) J Mater Sci 45:3242. doi:10.1007/s10853-010-4331-9
25. Garvie RC, Gross MF (1986) J Mater Sci 21:1253. doi:10.1007/BF00553259
26. Wang ML, Wang CH, Wang W (2007) J Mater Chem 17:2133
27. Blin JL, Leonard A, Yuan Z, Gigot L, Vantomme A, Cheetham AK, Su BL (2003) Angew Chem Int Ed 42:2872
28. Langford JI, Wilson AJC (1978) J Appl Crystallogr 11:102
29. Jayaram V, Levi CG, Mehrabian R (1990) Mater Sci Eng A 124:65
30. Gao L, Qiu L, Hong JS, Miyamoto H, De La Torre SD, Kakitsuji A, Liddell K, Thompson DP (1998) J Mater Sci 33:1399. doi:10.1023/A:1004327104481
31. Trinh DH, Högberg H, Andersson JM, Collin M, Reineck I, Helmersson U, Hultman L (2006) J Vac Sci Technol A 24:309
32. Klimova T, Rojas ML, Castillo P, Cuevas R, Ramírez J (1998) Microporous Mesoporous Mater 20:293